Global stability prediction of compression ramp flow based on deep neural networks

Yuan Jia[a], Chih-Yung Wen[a], Chenjia Ning[b], Chi Zhang[a], Xu Wang[c], Zhengtong Li[a,*]

[a]*Department of Aeronautical and Aviation Engineering, The Hong Kong Polytechnic University, Hong Kong*
[b]*School of Aeronautics, Northwestern Polytechnical University, 710072, Xi'an, People's Republic of China*
[c]*Department of Mechanical Engineering, The Hong Kong Polytechnic University, Hong Kong*

Abstract

Deep neural networks incorporating an AutoEncoder architecture are applied to compression ramp flow with shock-wave/boundary-layer interaction. This study aims to demonstrate how the fusion of aerodynamic data distributed over the compression ramp surface enables global stability predictions of compression ramp flow using high-fidelity data from small datasets, thereby significantly reducing data acquisition costs. The deep learning model is trained on direct numerical simulations (DNS) of supersonic to hypersonic compression ramp flows, with global stability assessed using global stability analysis (GSA). The predictions agree well with experimental data and numerical simulations across a wide range of freestream Mach numbers, Reynolds number, far field flow temperature, ramp angle of the geometry and wall temperature ratio. Furthermore, by leveraging feature extraction techniques to train the model on a limited set of critical data points, the results remain highly accurate. This highlights an effective approach for optimizing sensor quantity and placement to evaluate the global stability of

*Corresponding author: Zhengtong Li (zheng-tong.li@polyu.edu.hk)

flows.

Keywords: Supersonic/Hypersonic data fusion, Compression ramp, Global stability, Feature extraction

1. Introduction

Hypersonic vehicles possess a significant application value due to their high speed, strong maneuverability, ultra-long range, and rapid response characteristics [1]. Therefore, they have become a research hotspot in the aerospace field worldwide [2]. However, as a high-dynamic, strongly coupled, rapidly varying, and uncertain multi-variable nonlinear system [3], accurately assessing and predicting the aerodynamic performance of hypersonic vehicles is a key challenge [4]. As a fundamental geometric feature widely applied in components of hypersonic vehicles such as wings, engine inlets, and junctions, compression ramps often involve flows accompanied by shock wave/boundary layer interactions (SWBLI) [5], and several experiments [6, 7, 8, 9, 10] have been conducted to study them. As shown in Figure 1, the separated flow induced by shock waves interacts with the upstream laminar flow, being highly sensitive to upstream disturbances and capable of supporting self-sustaining global instabilities [11]. Downstream of flow

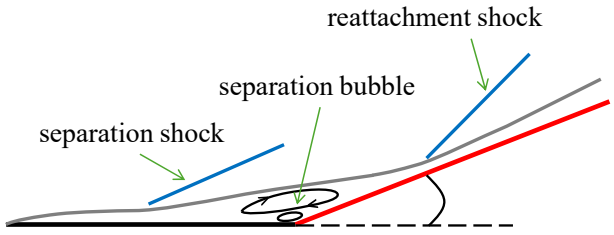

Figure 1: Schematic of the supersonic/hypersonic flow features over a compression ramp.

reattachment, streamwise stripes are often observed, leading to a significant increase in peak heating and a strong lateral variation of flow feature that promote boundary layer transition downstream of reattachment [12].

When considering laminar interactions, the dynamics of shock wave/laminar boundary layer interaction (SLBLI) system can be viewed as an oscillator or a noise amplifier. For oscillator flows in SLBLI flows, the intrinsic mechanism has been observed . In these cases, Global Stability Analysis (GSA) and direct numerical simulation (DNS) have been utilized to investigate the evolution of the spanwise wavelength. A consistent linear growth rate was observed between the most unstable mode identified by GSA and the temporal DNS history of the physical properties, indicating that the flow's early-stage unsteadiness arises from intrinsic global instability. In contrast, for noise-amplifier flows in SLBLI flows, external disturbances are amplified through convective mechanisms, as demonstrated by the resolvent analysis. The resolvent analysis reveals that the formation of streamwise streaks is a consequence of upstream disturbances being amplified. In the case of turbulent interactions, as the incoming turbulent boundary layer can be regarded as one type of external disturbance acting on the separation flow, it is believed that the the dynamics of the shock wave/turbulent boundary layer interaction (STBLI) flows is in a convective way [13]. The corresponding separated shock waves often undergo oscillatory motions, with a fundamental frequency that is much lower than that of the energetic eddies in the incoming boundary layer [14]. This low-frequency, large-scale instability can have adverse effects on the vehicle's structure and lead to a decline in performance [15]. Therefore, it is crucial to enhance the prediction of global instabilities in both laminar and turbulent SWBLI in order to better control the low-frequency unsteady motion of

the shock system and reduce the risk of performance degradation in hypersonic vehicles.

Deep learning is widely used in engineering to create surrogate models that provide valuable insights and serve as cost-effective tools for optimization and interpretable AI [16, 17, 18]. Its application in aerospace has led to significant performance improvements [19]. In addition, it has been investigated that the use of the deep learning method for the reconstruction of pressure fluctuations in supersonic excitation boundary layer interactions [20]. Surrogate models based on deep learning can also improve predictions of global instabilities in compression ramps. However, their accuracy depends on the quality and amount of expensive data, such as DNS [21]. High data costs can limit model accuracy. This paper focuses on using a small high-fidelity dataset to predict global stability of compression corner flow, reducing reliance on large datasets. Several branches of deep learning have begun to address this issue. These efforts have varied from probabilistic models which provide uncertainty estimations [22], white-box models [23], physics-based deep learning [24, 25, 26], and transfer learning [27]. Recently, the fields of data fusion have significantly influenced the development of efficient and accurate surrogate models under limited data conditions [28, 29]. They are capable of identifying and integrating data from different sources or heterogeneous data from the same source. Therefore, through data fusion, different aerodynamic data can work closely together and complement each other, forming a closed loop that enhances the quality and efficiency of aerodynamic research while broadening its applicability [30].

He et al. [31] used deep neural networks (DNN) to combine multi-fidelity aerodynamic data, producing more high-quality data at lower cost. They found

that compared to traditional Kriging methods, DNN-based fusion works better for high-dimensional or large-scale data. Li et al. [32] developed a multi-fidelity DNN model using a large amount of low-fidelity data and a small amount of high-fidelity data, which predicted surface pressure on transonic wings more accurately than single-fidelity DNNs. Ning and Zhang [33] proposed MHA-Net, a method that fuses aerodynamic data from a single source by embedding reduced-dimensional features, improving model accuracy with small datasets. These studies show that data fusion is a promising approach in data-driven aerodynamic modeling, helping to balance accuracy and data costs while advancing high-quality, cost-effective aerodynamic databases.

This study aims to demonstrate how fusing distributed aerodynamic data over a compression ramp surface can facilitate high-fidelity data from a small dataset to predict the global stability of compression ramp flow, thereby significantly reducing data acquisition costs. Although there have been some studies on data fusion using deep learning, there remains significant potential for exploration when combined with the current task:

1. Current AI-based data fusion frameworks have mainly been used to predict aerodynamic forces on airfoils but have not yet been applied to global instability problems. While aerodynamic forces can be obtained from CFD or wind tunnel tests using simple geometric and flow parameters, predicting global instability requires analyzing the stability of small disturbances on a flow, which involves more complex, high-dimensional data. Also, existing frameworks focus on regression tasks for force prediction, whereas global instability prediction is a binary classification problem. Our goal is to modify these AI frameworks to see if a small, high-quality dataset can accurately predict the global stability of compression cor-

ner flow. We will also check if the AI predictions match well with experimental data and simulations across various Mach numbers, flow temperatures, ramp angles, and other conditions.

2. Previous data fusion frameworks have successfully combined overlooked distributed loads like airfoil surface pressure. For global flow instability over compression corners, two key distributed features are the skin friction coefficient and the surface pressure coefficient. We aim to find out which of these better improves instability prediction. Additionally, we will explore whether different types of distributed data have different impacts on prediction accuracy. From a data-driven perspective, we also want to see if the importance of these data types matches our physical understanding. If it does, we could choose which data to fuse based on physical knowledge instead of using all available data.

3. Previous frameworks fused surface pressure data from the entire wing. Here, we want to see if using data from the whole compression ramp is necessary or if some data points are redundant. We will investigate whether similar prediction accuracy can be achieved using only a few key data locations, which would reduce the number of sensors and lower data collection costs. Additionally, we will check if the importance of these key locations matches our physical understanding. If so, we can select important data points based on physical knowledge instead of using all data. This paper focuses on these questions to extend data fusion methods for predicting global flow instability in supersonic/hypersonic laminar SWBLI conditions.

The structure of this paper is as follows:

Section 2 introduces the data acquisition method and the DNN and AutoEncoder-based neural network (DA-Net) approach, outlining the components of DA-Net.

Section 3 tests DA-Net's performance with small datasets, evaluates different aerodynamic data types for fusion, and uses feature extraction to select key data points. Section 4 discusses using physical prior knowledge in DA-Net and tests its ability to generalize. Section 5 summarizes the main findings.

2. Dataset acquisition and Methodology

2.1. Dataset acquisition

The physical background of this study is the supersonic/hypersonic flow field and the data is obtained by numerical simulations using an in-house multi-block parallel finite-volume solver called PHAROS [34, 35], which have been validated before[11, 36]. The compressible Navier-Stokes equations for a calorically perfect gas in 2D is written in the following conservation form:

$$\frac{\partial \boldsymbol{U}}{\partial t}+\frac{\partial \boldsymbol{F}}{\partial x}+\frac{\partial \boldsymbol{G}}{\partial y}=\frac{\partial \boldsymbol{F}_v}{\partial x}+\frac{\partial \boldsymbol{G}_v}{\partial y}, \tag{1}$$

where $\boldsymbol{U}=(\rho,\rho u,\rho v,\rho e)^T$ is the vector of conservative variables, while $\boldsymbol{F}$ and $\boldsymbol{F}_v$ denote the vectors of inviscid and viscous fluxes in the x direction, respectively, given by:

$$\boldsymbol{F}=\begin{pmatrix}\rho u\\ \rho u^2+p\\ \rho uv\\ (\rho e+p)u\end{pmatrix},\quad \boldsymbol{F}_v=\begin{pmatrix}0\\ \tau_{xx}\\ \tau_{xy}\\ u\tau_{xx}+v\tau_{xy}-q_x\end{pmatrix}. \tag{2}$$

The parameters $\boldsymbol{G}$ and $\boldsymbol{G}_v$ can be expressed analogously. Here, ρ stands for density, u and v are the flow velocities in the x and y directions, respectively, p stands for pressure, e is the total energy per unit mass, τ_{ij} is the shear stress tensor modelled under the assumptions of a Newtonian fluid and Stokes' hypothesis,

and $\boldsymbol{q}$ is the heat conduction vector modelled by Fourier's law. Furthermore, the dynamic viscosity is evaluated by Sutherland's law. In our study, we focus on 2-D laminar simulations since the 2-D separated flow can bifurcate into three-dimensionality due to intrinsic instability [11, 37, 38, 39, 40].

As illustrated in Figure 2 [11], the geometry model consists of a flat plate with a length of $L = 100$ mm, followed by a ramp with various ramp angles. The free stream conditions encompass parameters such as the Mach number Ma, Reynolds number Re, far field flow temperature T_∞; Ramp angle α of the geometry and wall temperature ratio T_w/T_0, where T_w denotes wall temperature and T_0 is total temperature of far field flow. The variables ranges are as follows: $Ma \in 2 \sim 9.4$, $Re \in 3.36 \times 10^6 \sim 5.04 \times 10^6$, $T_\infty \in 100$ K ~ 150 K, $\alpha \in 9^\circ \sim 18^\circ$ and $T_w/T_0 \in 0.036 \sim 0.86$. The Latin Hypercube Sampling method [41] is employed to screen the parameter space, selecting 132 diverse parameter combinations for the computational analysis. After defining the geometric conditions α for modeling, simulations are conducted using PHAROS under the predefined computational settings. In our previous research [11], we have validated grid independence and confirmed its agreement with experimental data. Based on this, the current study employs this grid with refinement of 1200×400 in the streamwise and wall-normal directions. The grid has a normal spacing of 1×10^{-7} at surfaces.

The locations of 2D CFD measurement points in Figure 2 for data fusion are just like sensors to measure the local pressure and friction coefficients in the wind-tunnel experiments. A total of 39 points are selected at intervals of 0.05 between $x/L = 0.05$ and $x/L = 1.95$ along the ramp surface, capturing the values of the points' friction coefficient C_f and pressure coefficient C_p. The C_f and C_p are

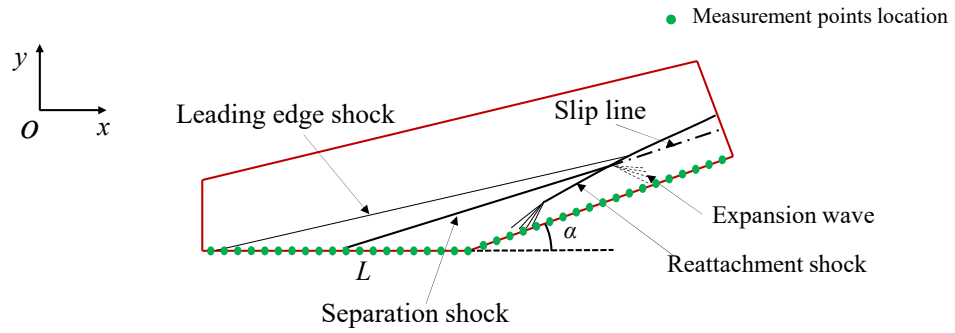

Figure 2: Computational domain for the 2D compression ramp flow simulation bounded by red lines, where the measurement points for skin friction and pressure are depicted by green dots on the wall and the flow structure is also presented.

defined by

$$C_f = \frac{2\tau_w}{\rho_\infty u_\infty^2}, C_p = \frac{2p_w}{\rho_\infty u_\infty^2}, \tag{3}$$

where ρ_∞ is the density, u_∞ is the velocity, τ_w and p_w are the wall shear stress and pressure. The calculation results of the points' surface coefficients are integrated into the supersonic/hypersonic data part.

Finally, the flow field data obtained through PHAROS calculations will be subjected to GSA to assess the global stability concerning periodic spanwise perturbations. Within the GSA method, the vector of conservative variables $\hat{\boldsymbol{U}}$ is partitioned into a 2-D steady solution $\boldsymbol{U}_{2-\mathrm{D}}$ and a 3-D small-amplitude perturbation represented by $\boldsymbol{U}'$:

$$\boldsymbol{U}(x,y,z,t) = \boldsymbol{U}_{2-\mathrm{D}}(x,y) + \boldsymbol{U}'(x,y,z,t). \tag{4}$$

To transform it to an eigenvalue problem, $\boldsymbol{U}'$ can be further expressed in the

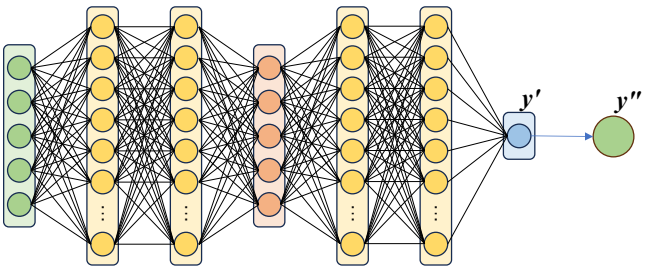

Figure 3: The architecture of DNN method.

following modal form:

$$\boldsymbol{U}'(x,y,z,t) = \hat{\boldsymbol{U}}(x,y)\exp\left(-\mathrm{i}\omega t + \mathrm{i}\frac{2\pi}{\lambda}z\right), \tag{5}$$

where $\hat{\boldsymbol{U}}$ is the 2-D eigenfunction, ω is the eigenvalue and λ is the spanwise wavelength.

In our study, after extracting the critical regions with a total of 210,000 grids for determining flow stability, computations using the GSA method across 8 different wavelengths on Intel(R) Core(TM)i7-14700K CPU require approximately 4 hours to ascertain the stability of a flow field.

2.2. Deep neural network for global instability prediction

We first construct a deep learning model based on DNN for global instability prediction, as shown in Figure 3. The DNN takes as input far-field inflow conditions, wall temperature ratio, and ramp geometry parameters, including Ma, Re, T_∞, T_w/T_0 and α. The DNN employs binary classification, so the initial output $\boldsymbol{y'}$ is the possibility of being unstable. The initial output $\boldsymbol{y'}$ is generated through the sigmoid function, which confines the $\boldsymbol{y'}$ range between 0 and 1. Subsequent processing is applied to $\boldsymbol{y'}$ to derive the final output $\boldsymbol{y''}$ that only contains two results:

$'0'$ (stable) or $'1'$ (unstable). This DNN does not incorporate surface distribution data of the compression corner; it will serve as a benchmark for comparison with the data fusion methods discussed later.

2.3. *DNN and AutoEncoder-based neural network (DA-Net) for global instability prediction*

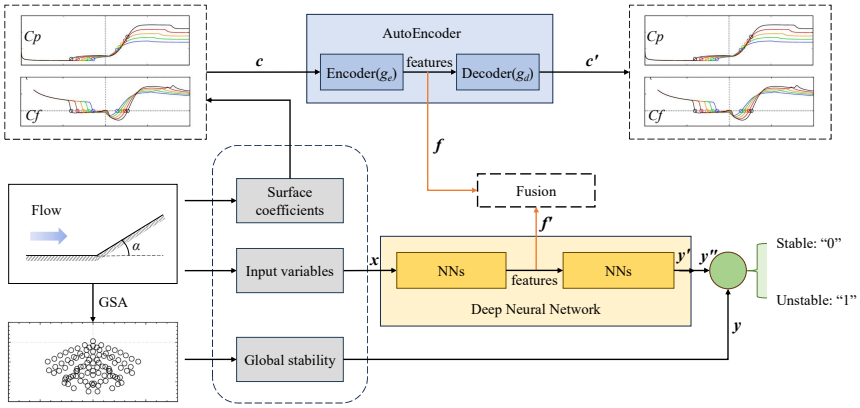

Figure 4: The flowchart of DA-Net.

We further integrate the DNN and AutoEncoder to form DA-Net. This DA-Net, based on the benchmark established in Section 2.2, enables the further fusion of two different types of data, C_f and C_p, obtained from high-fidelity DNS simulations. As illustrated in Figure 4, each sample set is divided into three parts in DA-Net: input variables $\boldsymbol{x}$ (Ma, Re, T_∞, T_w/T_0 and α), surface coefficients $\boldsymbol{c}$ (C_f and C_p) and the ground truth of flow field stability outcome $\boldsymbol{y}$ by GSA. The outcome $\boldsymbol{y}$ has two possibilities, $'0'$ signifies a globally stable flow field, while $'1'$ indicates a globally unstable flow field. For example, initially, the pressure coefficients and friction coefficients of 39 points collectively form surface coefficients $\boldsymbol{c}$

from 2D CFD; Subsequently, the pressure coefficients and friction coefficients of the 39 points are input as $\boldsymbol{c}$ individually; Finally, a selection of surface coefficients from specific points will be extracted for $\boldsymbol{c}$ input.

The AutoEncoder (AE) is applied in the DA-Net for including data and feature extraction of pressure coefficients or friction coefficients. It is composed of two main parts: encoder and decoder, for unsupervised learning. As is shown in

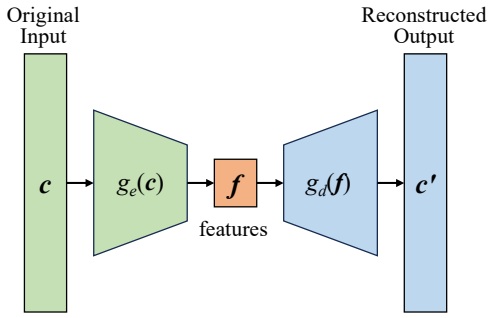

Figure 5: The structure of AutoEncoder.

Figure 5, initially, The encoder takes input $\boldsymbol{c}$ of surface coefficients and extracts latent space's features $\boldsymbol{f}$ by function of $g_e(\boldsymbol{c})$, the decoder takes the latent space representation $\boldsymbol{f}$ and reconstruct the original input data to $\boldsymbol{c'}$ by function of $g_d(\boldsymbol{f})$. The mathematical computation formula for this process is as follows:

$$\boldsymbol{f} = g_e(\boldsymbol{c}), \tag{6}$$

$$\boldsymbol{c'} = g_d(\boldsymbol{f}). \tag{7}$$

The DNN segment follows the same benchmark practice of the DNN-based data prediction method described above. The intermediate result $\boldsymbol{f'}$ maintains the same dimensions as the encoder output $\boldsymbol{f}$, allowing the dimension-reduced

features of surface coefficients $\boldsymbol{f}$ to be integrated into the supersonic/hypersonic model, thereby facilitating data fusion.

The overall loss of DA-Net is comprised of the following three parts:

$$L = \lambda_1 L_y + \lambda_2 L_{AE} + \lambda_3 L_{\boldsymbol{f}}, \tag{8}$$

where λ_1, λ_2 and λ_3 are loss weight factors. The first component of DA-Net driven by the predicted possibility of flow field instability $\boldsymbol{y'}$ and $\boldsymbol{y}$:

$$L_y = \frac{1}{N}\sum_{i=1}^{N}(\boldsymbol{y'} - \boldsymbol{y})^2. \tag{9}$$

The second component of DA-Net comprises the input $\boldsymbol{c}$ and output $\boldsymbol{c'}$ of the AE:

$$L_{AE} = \frac{1}{N}\sum_{i=1}^{N}(\boldsymbol{c'} - \boldsymbol{c})^2. \tag{10}$$

The third component of DA-Net is due to the extracted reduced features:

$$L_f = \frac{1}{N}\sum_{i=1}^{N}(\boldsymbol{f'} - \boldsymbol{f})^2. \tag{11}$$

In L_f training loss, the first term $\boldsymbol{f'}$ is the feature of initial flow conditions, which determine the base flow of a global state; the second term $\boldsymbol{f}$ focuses on flow field feature extraction, extracting surface pressure or friction coefficients closely related to the flow field separation as well as flow instability, which is more related to the local field. The difference between these two terms is the direct modeling of the strength of local imbalances in flows, which are the triggers of instability.

In this research, the Adam optimizer [42] and adaptive learning rate optimization techniques for stochastic gradient descent are implemented to minimize training errors.

2.4. Results evaluation

As predicting global stability is a binary classification problem, accuracy, precision, mean squared error (MSE) and mean absolute error (MAE) are employed to evaluate the method's performance comprehensively. The MAE, MSE, accuracy and precision of sigmoid function are defined by following equations:

$$MAE = \frac{1}{N}\sum_{i=1}^{N}|\boldsymbol{y}' - \boldsymbol{y}|, \tag{12}$$

$$MSE = \frac{1}{N}\sum_{i=1}^{N}(\boldsymbol{y}' - \boldsymbol{y})^2, \tag{13}$$

$$Accuracy = \frac{TP+TN}{TP+TN+FP+FN}, \tag{14}$$

$$Precision = \frac{TP}{TP+FP}, \tag{15}$$

where True Positive (TP) is the number of instances that are actually positive (globally unstable) and are correctly predicted as positive; True Negative (TN) is the number of instances that are actually negative (globally stable) and are correctly predicted as negative; False Positive (FP) is the number of instances that are actually negative but are incorrectly predicted as positive; False Negative (FN) is the number of instances that are actually positive but are incorrectly predicted as negative. In general, accuracy measures the percentage of correct predictions out of all predictions, reflecting how well both globally stable and unstable cases are identified; Precision is the ratio of correctly predicted positive cases to all predicted positives, indicating how many predicted unstable flows are truly unstable.

3. Results

3.1. General flow features and occurrence of global instability

Through our research, we find that general flow features are closely related to the occurrence of global instability. Figures 6 to 7 show the base flow visualized using Mach number contour and distribution of skin friction coefficients on the 2D ramp, with initial conditions of $Ma = 7.7$, $Re = 4.2 \times 10^6$, $\alpha = 15°$, $T_\infty = 125$ K and wall temperature ratio $T_w/T_0 = 0.045$. Due to the pressure rise, the separation bubble formed near the compression corner. The separation shock interacts with the reattachment shock, leading to the expansion wave and slip line (see Figure 2). From the enlarged view of skin friction, it can be seen that near the compression corner, there is a $'$local peak$'$ between two minimum skin friction coefficients. From previous research [11], it was demonstrated that when the $'$local peak$'$ is positive, the flow field has secondary separation and becomes globally unstable. Therefore, it indicates that when the flow field under global instability, there is a certain variation in the friction coefficient inside the separation bubble near the compression corner. Figure 8 and Figure 9 show the distribution of pressure co-

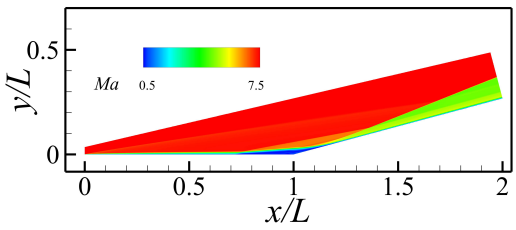

Figure 6: Base-flow visualization for ramp with $Ma = 7.7$, $Re = 4.2 \times 10^6$, $\alpha = 15°$, $T_\infty = 125$ K and wall temperature ratio $T_w/T_0 = 0.045$.

efficients and pressure gradient dC_P/dx^* (x^* is the non-dimensional distance from

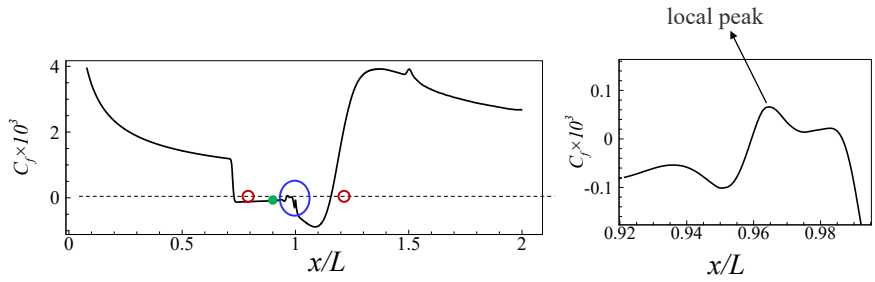

Figure 7: Distribution of skin friction coefficients for ramp with $Ma = 7.7$, $Re = 4.2 \times 10^6$, $\alpha = 15°$, $T_\infty = 125$ K and wall temperature ratio $T_w/T_0 = 0.045$; Red circles: separation and reattachment points; Blue circle: the enlarged view part; Green point: $x/L = 0.85$ inside the separation bubble.

the leading edge) along the 2D ramp respectively, with initial conditions of $Ma = 5.2$, $Re = 3.4 \times 10^6$, $\alpha = 13°$, $T_\infty = 146$ K and wall temperature ratio $T_w/T_0 = 0.25$. Overall, the surface pressure increases upstream of the separation point controlled by the free-interaction process. This rise is followed by a plateau region, the value of which increases with α and T_w/T_0. The pressure rises again near the reattachment point and reaches its peak value mainly determined by the oblique shock theory. The drop in C_p downstream of the peak is caused by the impingement of expansion wave (see Figure 2). It can be also seen that near the compression corner, there is a $'$local dip$'$ between the pressure plateau part and $'$pressure rises$'$ part, with the $'$pressure rises$'$ part exhibiting a significant pressure gradient. The $'$ dip$'$ is indicative of a local region with pressure gradient near the corner, which becomes stronger as α is increased such that the reverse flow boundary layer cannot resist it and gives rise to secondary separation. Notably, this phenomenon prevails for different initial conditions. The distribution characteristics of surface pressure and surface friction to some extent imply the linkage to the possibility of

global instability. This inspires us to incorporate this flow physics information

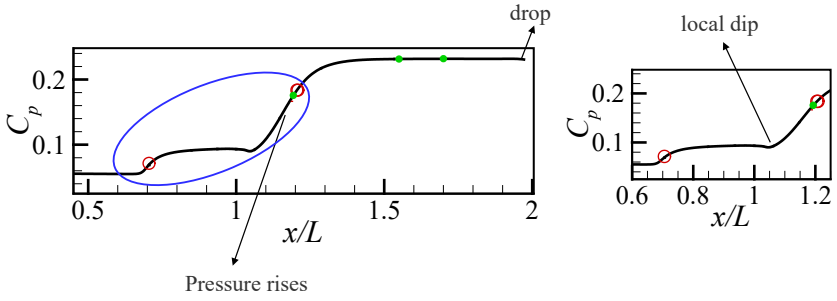

Figure 8: Distribution of pressure coefficients for ramp with Ma = 5.2, Re = 3.4 $\times 10^6$, α = 13°, T_∞ = 146 K and wall temperature ratio T_w/T_0 = 0.25; Red circles: separation and reattachment points; Blue circle: the enlarged view part; Green points: $x/L = 1.2$ inside the separation bubble, $x/L = 1.55$ and $x/L = 1.7$ in the pressure peak part.

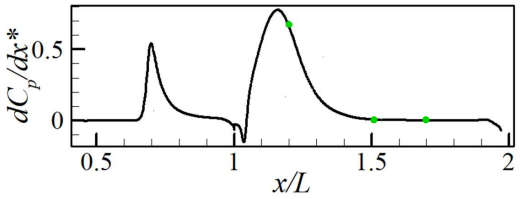

Figure 9: Distribution of surface pressure gradient for ramp with Ma = 5.2, Re = 3.4 $\times 10^6$, α = 13°, T_∞ = 146 K and wall temperature ratio T_w/T_0 = 0.25; Green points: $x/L = 1.2$ inside the separation bubble, $x/L = 1.55$ and $x/L = 1.7$ in the pressure peak part.

into neural network training, which not only enhances the interpretability of the surrogate model but also reduces its reliance on large datasets during training.

3.2. Comparison of DNN-based method and DA-Net data fusion method

We will test the two methods introduced in Section 2.2 and 2.3 to evaluate their performance in predicting global stability across datasets of different sizes.

This will allow us to assess the data fusion method, specifically the advantage of our proposed DA-Net, on small-sample datasets. The entire dataset comprises 132 samples, as detailed in Section 2.3, consisting of Ma, Re, T_∞, α, T_w/T_0, and data for fusion: C_p and C_f of 39 points on the surface of the compression corner. The dataset is randomly split into two parts: 112 cases ($\backsim$ 85%) are used as the training set and validation set, and the remaining 20 cases ($\backsim$15%) are allocated for testing. Within the training set, 10% is randomly sampled as the validation set (accounting for 8.5% of the total dataset) to optimize the hyperparameters.

In the previous studies on triple-deck theory [43, 44], the scaled ramp angle α^*[43] can be expressed by the following equation.

$$\alpha^* = \frac{\alpha Re^{1/4}}{C^{1/4} 0.332^{1/2} \left(Ma^2 - 1\right)^{1/4}}, \quad C = \frac{\mu_w T_\infty}{\mu_\infty T_w}, \tag{16}$$

where C is the Chapman–Rubesin parameter, μ_w and μ_∞ are the dynamic viscosity of wall and free stream flow. The criterion can be established in terms of α^* to predict the stability boundary. As shown in Figure 10 [11] (modified from [11]), the α^* range of demarcation between global stable and global unstable flows is from 3.44 to 4.59, depending on the wall temperature ratio. A higher wall temperature and large Reynolds number result in a larger critical ramp angle [43, 11, 36]. Therefore, We adjust the test dataset so that 85% of it falls within this range to validate the superiority of the method. Table 1 displays the optimized hyperparameters and in order to compare the impact of multiple data on the results, DNN maintains consistency with the parameters in DA-Net. In this table, the second and third columns represent the layer structure of the DNN part and AutoEncoder, respectively, indicating the number of neurons in each layer; The fourth column L_2 is the regularization coefficient, which indicates the strength of the penalty on the weights during training to prevent overfitting; The fifth column contains loss

Table 1: The hyperparameters of NNs.

Method	DNN	AutoEncoder	L2	$\{\lambda_1, \lambda_2, \lambda_3\}$	Batchsize
DA-Net	(5,32,12,32,1)	(78,32,16,12,16,32,78)	0.004	{0.5,2,1}	2
DNN	(5,32,12,32,1)		0.004		2

weight factors and the last column represent batchsize, indicating the number of data samples input to the network for each training.

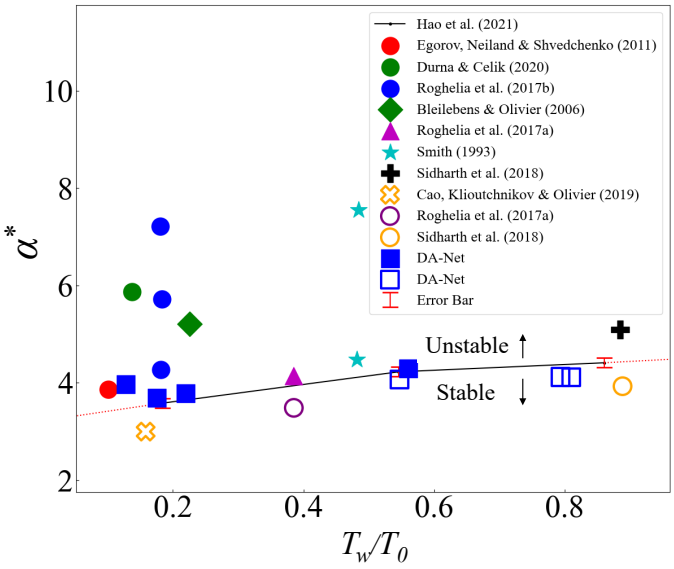

Figure 10: The critical ramp angle for global instability (modified from [11], Open Access, under Creative Commons CC BY license)[11, 45, 46, 47, 48, 6, 7, 8], where open symbols represent global stability and closed symbols represent global instability. DA-Net represents parts of prediction results of the DA-Net model.

Table 2 displays the comparison of prediction results between DNN-based method and DA-Net data fusion method under various training set proportions ranging from 10% to 90% (10% $\backsim$ 11 cases, 20% $\backsim$ 22 cases, 30% $\backsim$ 34 cases, 40% $\backsim$ 45 cases, 50% : 56 cases, 60% $\backsim$ 67 cases, 70% $\backsim$ 78 cases, 80% $\backsim$

Table 2: Results comparison of DNN and DA-Net

Training set proportion	DNN				DA-Net			
	MMSE	MMAE	Accuracy	Precision	MMSE	MMAE	Accuracy	Precision
10%	0.161914	0.360646	0.730	0.810270	0.075926	0.141433	0.875	0.954842
20%	0.102781	0.259459	0.890	0.905545	0.049732	0.098864	0.935	0.955452
30%	0.062735	0.211149	0.965	0.976471	0.037254	0.049236	0.960	1
40%	0.081098	0.241607	0.955	0.957778	0.010272	0.021429	0.985	1
50%	0.061713	0.206326	0.950	0.950221	0.022097	0.037308	0.965	1
60%	0.049839	0.194860	0.990	1	0.013291	0.022440	0.980	1
70%	0.065928	0.226843	0.980	0.978328	0.004550	0.012397	0.990	1
80%	0.043870	0.176104	0.980	0.994118	0.015839	0.023729	0.985	1
90%	0.081382	0.248061	0.970	0.968235	0.011718	0.026413	0.970	1

90 cases, 90% $\backsim$ 101 cases). Notably, when the training set proportion reaches 60% and above, the DNN-based method achieves accuracy of 0.97 or even 0.99, showing that utilizing the deep learning method enables precise predictions within the restricted range of the triple-deck theory. We further compare the data fusion method with the DNN-based method and find that in both MMSE and MMAE, the DA-Net approach largely reduces prediction errors. The MMSE of DA-Net almost halves in comparison to the DNN-based method. Specifically, when the training set constitutes 40%, the MMSE decreases from 0.0810978 to 0.010272, shrinking by over 8 times. Figure 11 illustrates the box plot of MAE with a training set percentage of 70%, the MMAE for 10 times decreases from 0.22684 to 0.0124 , reduced by nearly 94.5%. Meanwhile, the median line and range for DA-Net decreases a lot compared to the DNN, indicating DA-Net exhibits an improved model dispersion.

As depicted in Figure 12, the DA-Net data fusion method exhibits superior predictive accuracy over the DNN-based method, particularly in scenarios with limited training data, showcasing a 19.9% improvement in accuracy when the

training set is only 10%. Across all training set proportions, the data fusion method consistently outperforms the DNN in terms of precision, underscoring the exceptional benefits and effectiveness of this approach.

Furthermore, once the surrogate model is established by DA-Net, predicting the stability of a flow field on Intel(R) Core(TM) i7-14700K CPU typically demands just a fraction of a second, reducing the time by approximately 5 orders of magnitude and saving computational resources compared to the GSA method.

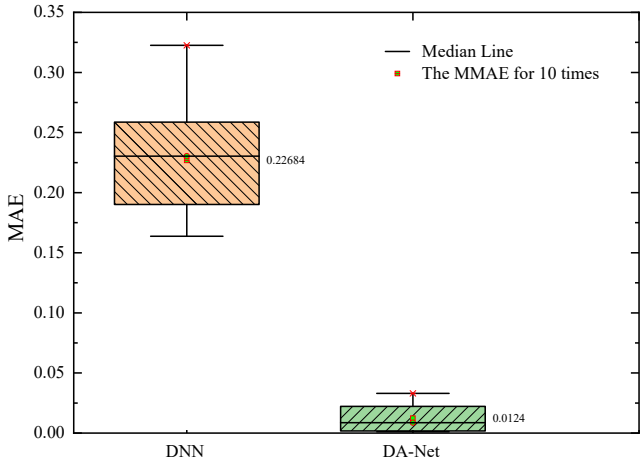

Figure 11: The MAE on the test set with the training set comprising 70% of the dataset.

3.3. Effect of data type for prediction results of DA-Net

In section 3.2, both C_f and C_p are integrated into DA-Net. To further reduce data dependency, this section separately introduces these two coefficients to investigate their influence on the stability prediction results. Table 3 lists the optimized hyperparameters applied in this section. Table 4 lists the DA-Net results comparison with C_p or C_f data alone. Figure 13 displays box plots comparing the utilization of C_p and C_f as input variables across different training set sizes. It

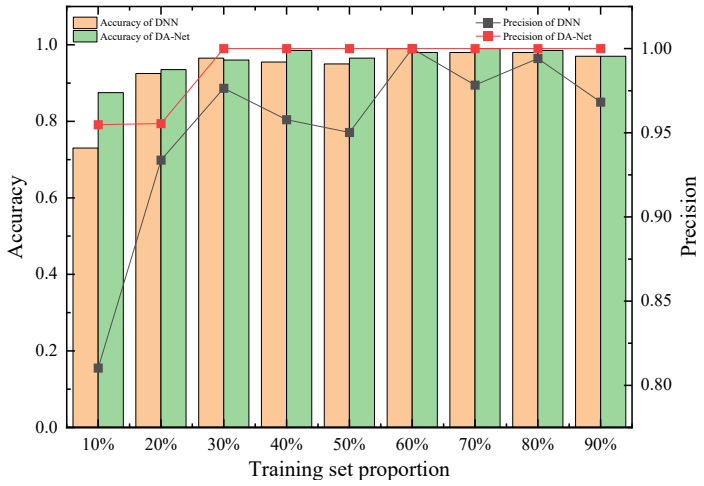

Figure 12: Accuracy and precision comparison between DNN-based method and DA-Net with data of both C_f and C_p.

Table 3: The hyperparameters of NNs.

Method	DNN	AutoEncoder	L2	$\{\lambda_1, \lambda_2, \lambda_3\}$	Batchsize
DA-Net	(5,32,12,32,1)	(39,32,16,12,16,32,39)	0.004	{0.5,2,1}	2

is evident that when using less than 50% training set, integrating pressure coefficients as input variables into DA-Net results in smaller MMAE than skin friction coefficients, leading to a reduction in prediction errors. The MAE difference becomes less significant when using more than 50% training set. Figure 14 displays the comparison of prediction results between DA-Net with data of C_f (DA-Net (C_f))and DA-Net with data of C_p (DA-Net (C_p)) under varying training set proportions ranging from 10% to 90%. It can be observed that in small training set samples, the latter achieves a higher accuracy and when the training samples are large, they have similar accuracy. Meanwhile, the precision of (C_p) as input vari-

Table 4: DA-Net results with C_f or C_p data alone

Training set proportion	DA-Net(C_f)				DA-Net(C_p)			
	MMSE	MMAE	Accuracy	Precision	MMSE	MMAE	Accuracy	Precision
10%	0.112242	0.248249	0.785	0.803757	0.110882	0.205599	0.835	0.841471
20%	0.116432	0.185247	0.870	0.957083	0.061515	0.075989	0.920	0.962819
30%	0.047055	0.064730	0.950	0.988889	0.019606	0.035336	0.975	0.994118
40%	0.036066	0.048799	0.960	0.983007	0.022975	0.034248	0.970	1
50%	0.022730	0.037542	0.965	1	0.021377	0.035530	0.970	0.994118
60%	0.016852	0.028754	0.970	0.994118	0.027793	0.042469	0.970	1
70%	0.009495	0.022305	0.985	1	0.025605	0.043401	0.965	1
80%	0.007833	0.019122	0.990	1	0.005451	0.014511	0.995	1
90%	0.021249	0.037672	0.970	1	0.001710	0.010904	1	1

ables has larger precision in nearly all training set samples.

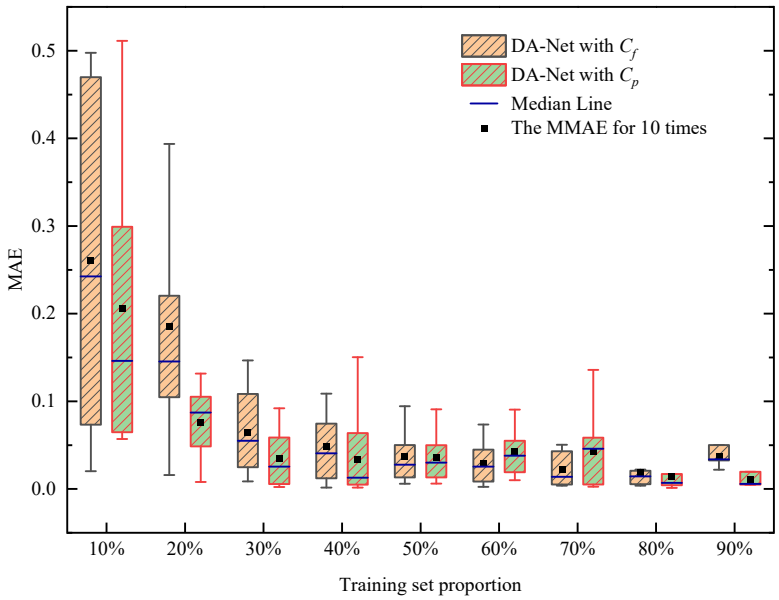

Figure 13: MAE change in predictions due to training sample modification with data of either C_f or C_p integrated in DA-Net.

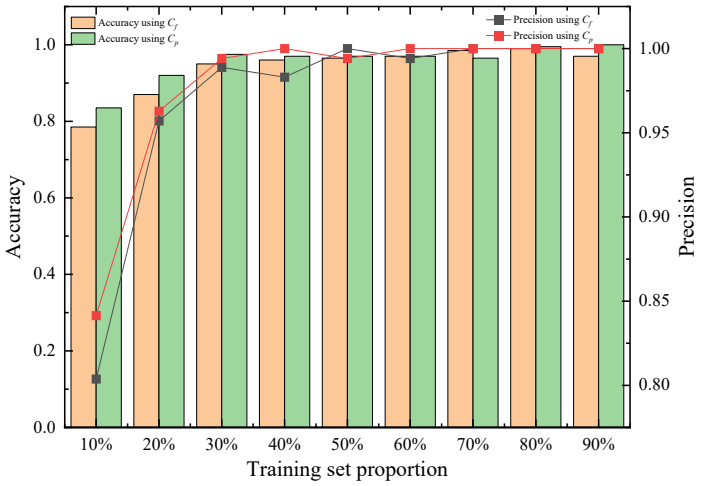

Figure 14: Accuracy and precision comparison between data of C_f and C_p integrated in DA-Net separately.

The adverse pressure gradient serves as one important factor contributing to flow separation. By analyzing the data, we can deduce that the integration of surface pressure coefficient has a more pronounced effect on result enhancement compared to that of friction coefficient. This observation aligns with the flow dynamics around the compression corner [11]. Consequently, in situations where the flow field exhibits global instability, such instabilities can be directly identified from the pressure-related data. In conclusion, we can utilize prior knowledge of physics to guide our selection of data type.

3.4. Effects of critical surface coefficients for prediction results of DA-Net

In Section 3.3, when only one type of distribution data from the compression corner surface is fused, DA-Net still demonstrates good predictive performance. However, the fused data covers the entire compression corner surface. If the dis-

tribution data is obtained from experimental measurements, it would significantly increase data acquisition costs. Therefore, in this section, data extraction method is utilized to select only a limited number of key data points on the compression corner surface for fusion. The SHapley Additive exPlanations (SHAP) [49] method is applied to extract the feature data of key points crucial for the global stability of the flow field. Figure 15 shows how each feature value impacts on predicting global stability. The x-axis illustrates the SHAP values, where a larger SHAP value indicates a more substantial impact on the outcomes. The y-axis, on the other hand, depicts the surface point's pressure coefficient or friction coefficient, with C_p : 1.7 indicating the surface pressure coefficient at $x/L = 1.7$.

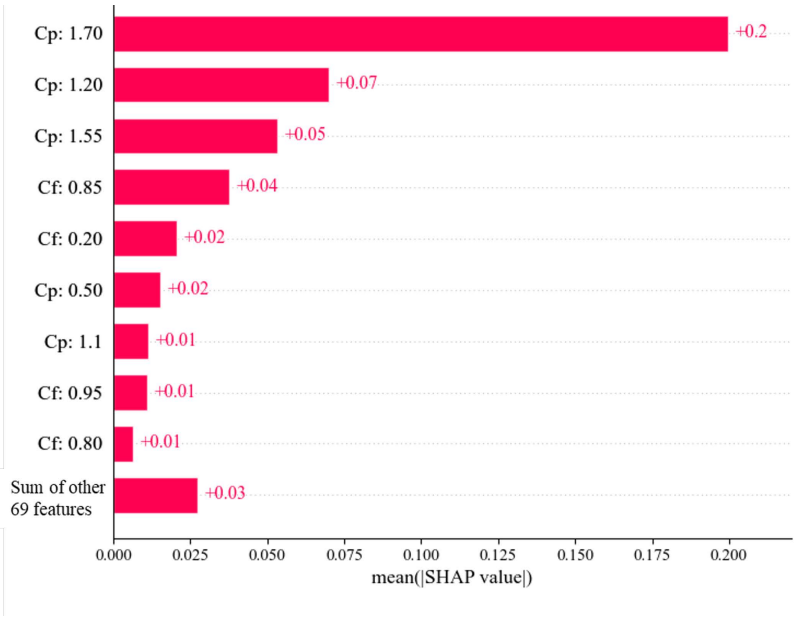

Figure 15: The direct impact of each feature on predicting global stability.

Upon examining these visuals, it becomes apparent that critical data influencing global stability includes the surface pressure coefficient post-separation region

Table 5: The hyperparameters of NNs for the case using extracted data in Sec.3.4.

Method	DNN	AutoEncoder	L2	$\{\lambda_1, \lambda_2, \lambda_3\}$	Batchsize
DA-Net	(5,32,12,32,1)	(4,32,16,12,16,32,4)	0.004	{0.5,2,1}	2

Table 6: DA-Net results with 4 key features data

Training set proportion	DA-Net			
	MMSE	MMAE	Accuracy	Precision
10%	0.108270	0.138041	0.870	0.914663
20%	0.060399	0.097505	0.935	0.987451
30%	0.047304	0.062195	0.950	0.957124
40%	0.021758	0.042853	0.975	0.981985
50%	0.014561	0.026088	0.980	0.988235
60%	0.004335	0.018311	1	1
70%	0.003271	0.012883	1	1
80%	0.002400	0.011226	1	1
90%	0.000700	0.009990	1	1

and the surface friction coefficient within the separation area near the compression corner. This observation aligns with the findings of Hao's study[11], where this specific region aligns with the $'$pressure gradient near corner$'$ and the largest pressure plateau phenomena. An increased pressure plateau signifies a heightened gradient near the corner, leading to global instability and subsequent secondary separation. Then, the top four influential features: the pressure coefficients at $x/L = 1.2, 1.55$ and 1.7 locations (near $'$ local dip$'$ and final pressure peak parts in Figure 8) , along with the friction coefficient at the $x/L = 0.85$ position (in the separation bubble the region near ramp corner in Figure 7), are selected as data

to investigate their impact on the prediction results. Table 5 lists the optimized hyperparameters employed in this section. Table 6 displays the prediction results of DA-Net when utilizing the data from the top four features as part of multiple data. It can be seen that the accuracy and precision is extremely high when the training set accounts for 60%, 70%, 80%and 90% of the total training cases (112 cases). Figure 16 shows the MAE comparison before and after feature extraction. It is evident that across the majority of training sets, models with feature extraction exhibit lower MAE, especially when the training set exceeds 50% of the total training cases.

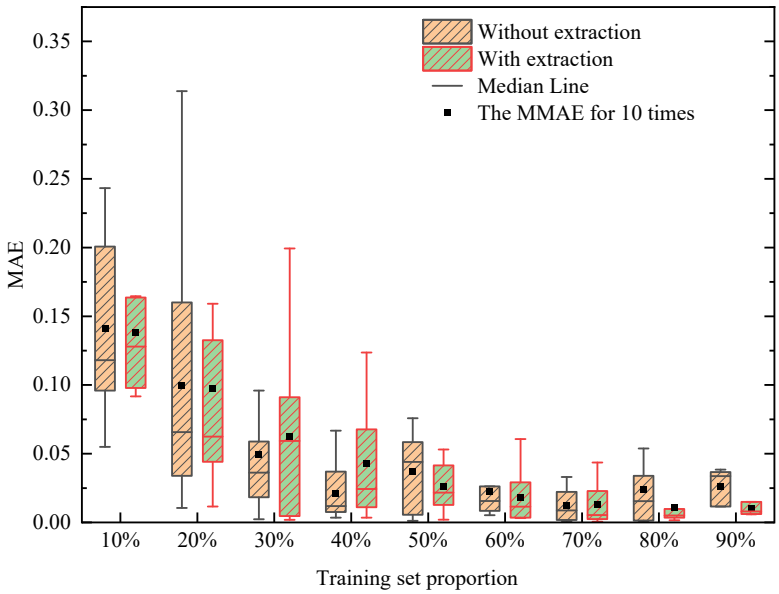

Figure 16: MAE comparison with and without feature extraction.

Figure 17 shows the accuracy and precision comparison with and without incorporating surface coefficients extraction. Upon feature extraction, accuracy im-

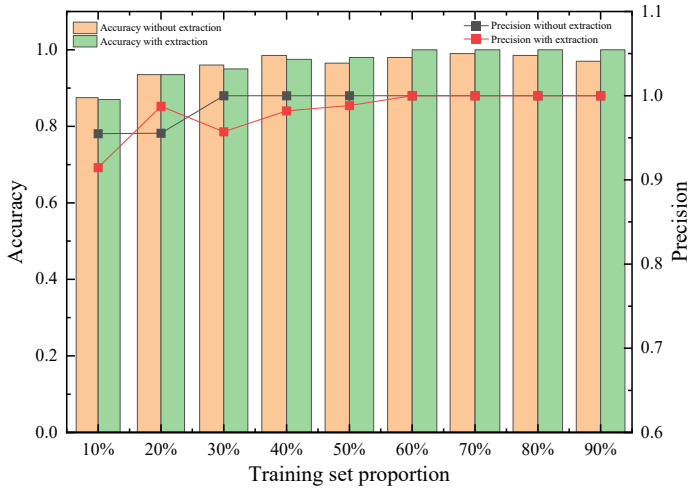

Figure 17: Accuracy and precision comparison with and without feature extraction.

proves across more than half of the training set ratios. Specifically, When the proportion of the training set is large (60%, 70%, 80% and 90%), there is a noticeable improvement in accuracy, reaching a value of 1. Moreover, it is observable that DA-Net can achieve a similar precision across varying sizes of training set samples. This indicates that utilizing feature-extracted data can achieve results comparable to or even better than inputting all data points of pressure and skin friction coefficients, fully exploiting the advantages of DA-Net's data fusion. Moreover, efficient data extraction can reduce data dependence and optimize the functionality of the DA-Net data fusion method.

4. Discussion

Drawing inspiration from Section 3.1, we incorporate the global distribution of pressure and friction measurements. Then, in Sections 3.2 – 3.4, from a data-

driven perspective, we identify the most important data types and key point locations, integrating them effectively into the surrogate model. In fact, through our previous numerical simulation studies [11],we have already summarized the critical data points and their corresponding data types. For instance, global instability of laminar SWBLI is closely linked with the emergence of secondary separation, and secondary separation can be manifested through the changes in the friction coefficient inside the separation bubble (near the ramp corner). So in this section, only the friction coefficient in the ramp corner at $x/L = 0.85$ (whcih is extracted is section 3.4) is applied for data fusion. This chapter uses the same optimized hyperparameters as before. Table 7 displays the prediction results of DA-Net when utilizing the friction coefficient C_f as part of source data and it can be seen that the accuracy and precision is extremely high when the training set accounts for 50%, 60%, 70%, 80% and 90%. Figure 18 shows the accuracy and precision with all the surface coefficients and with the corner friction coefficient only.

Subsequently, we further evaluate the extrapolation performance of the trained DA-Net. Specifically, we test the DA-Net model, which only utilizes corner C_f. The test set is selected from the experiments [6, 7, 8, 9, 10] summarized in Figure 10 on the compression ramp. Table 8 presents the parameters of these experiments shown in Figure 10, most of which are beyond the parameter space of training dataset ($Ma \in 2 \sim 9.4$, $Re \in 3.36 \times 10^6 \sim 5.04 \times 10^6$, $T_\infty \in 100$ K ~ 150 K, $\alpha \in 9^\circ \sim 18^\circ$ and $T_w/T_0 \in 0.036 \sim 0.86$). In Table 8, the parameters highlighted in red are beyond the parameter space of the training set. Table 9 shows the prediction results with the model only utilizing corner C_f. Figure 19 displays the accuracy and precision results for experiments at different training dataset ratios. It can be observed that when the training set is above 50%, the accuracy and precision can

Table 7: DA-Net results with corner friction coefficient data

Training set proportion	DA-Net			
	MMSE	MMAE	Accuracy	Precision
10%	0.127520	0.169239	0.840	0.915765824
20%	0.045705	0.076194	0.945	0.976339869
30%	0.046071	0.064311	0.945	0.960416667
40%	0.020335	0.050387	0.985	0.988235294
50%	0.011498	0.034611	1	1
60%	0.010072	0.024566	0.99	1
70%	0.010481	0.024313	0.99	0.988888889
80%	0.001550	0.010427	1	1
90%	0.001535	0.018917	1	1

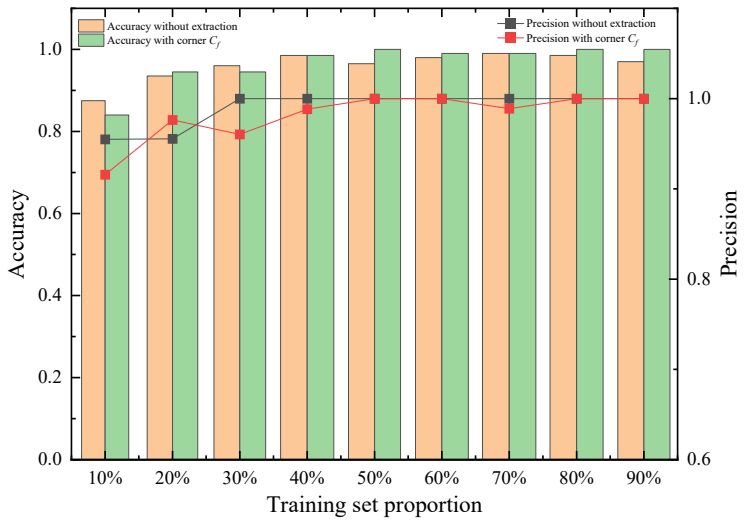

Figure 18: Comparison of accuracy and precision with full surface coefficients and with corner C_f only.

Table 8: Initial flow conditions of experiments (The parameters marked in red are beyond the initial parameter space).

References	Ma	Re_L	T_∞	α	T_w/T_0
[8]	6.85	380000	58.74	15°	0.49
[8]	6.85	380000	58.74	25°	0.49
[7]	7.7	420000	125	15°	0.18
[7]	7.7	420000	125	20°	0.18
[7]	7.7	420000	125	25°	0.18
[6]	8	200000	55	15°	0.39
[10]	7.7	760000	254	15°	0.22
[9]	11.63	240000	67	15°	0.16

reach 1 and therefore this model performs well in the experiment cases.

Further research is conducted on the 16 global instability cases in the test set. In the globally unstable case, 11 cases have secondary separation. This is consistent with the conclusion that the global instability occurs immediately prior to the emergence of the secondary separation [11]. Figure 20 presents the pressure contour normalized by $\rho_\infty u_\infty^2$ near the compression corner superimposed with streamlines in the separation region. In this case (Ma = 4.39, Re = 4.45×10^6, α = 12.1°, T_∞ = 135.35, T_w/T_0 = 0.24), the secondary separation has occurred in the compression corner. Next, the remaining five cases, in which no secondary separation occurs but global instability is dectected by DA-Net, are discussed. As illustrated in Figure 21 (Ma = 5.46, Re = 4.79×10^6, α = 11.7°, T_∞ = 123.74, T_w/T_0 = 0.56), when the ramp angle is 11.7°, the flow field does not exhibit secondary separation. But when the ramp angle is increased by 1° to 12.7°, as shown in

Table 9: DA-Net prediction results of with corner friction coefficient data for the experiments

Training set proportion	DA-Net			
	MMSE	MMAE	Accuracy	Precision
10%	0.117515	0.127086	0.875	1
20%	0.112308	0.131636	0.875	1
30%	0.138298	0.167775	0.875	1
40%	0.122856	0.131403	0.875	0.857
50%	0.004617	0.026307	1	1
60%	0.000007	0.000952	1	1
70%	0.006369	0.040808	1	1
80%	0.020099	0.064376	1	1
90%	0.013358	0.053200	1	1

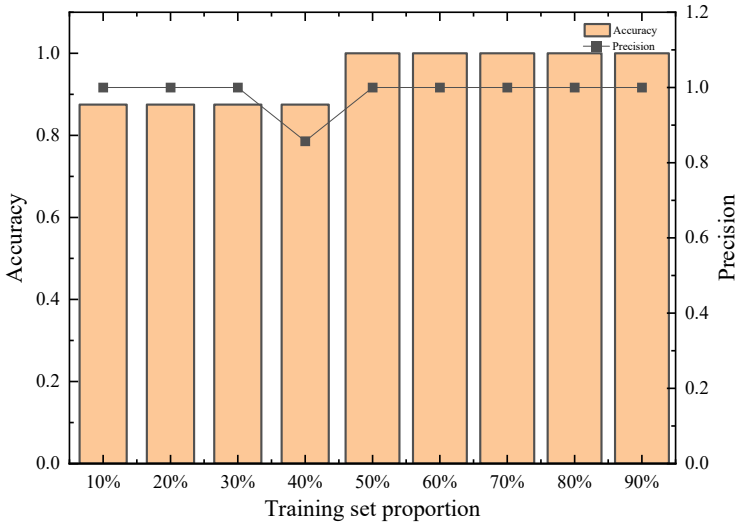

Figure 19: Accuracy and precision of experiments by using the model with corner C_f only.

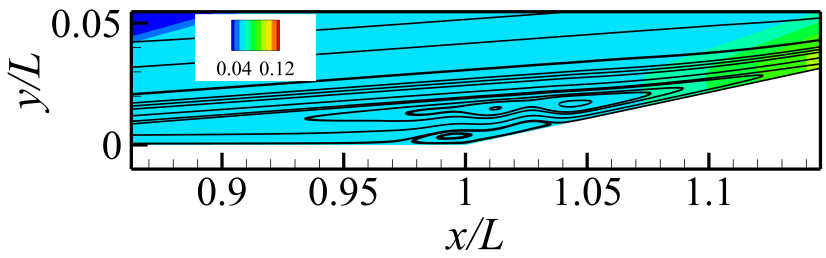

Figure 20: Non-dimensional pressure with streamlines around the compression corner ($Ma = 4.39$, $Re = 4.45\times10^6$, $\alpha = 12.1°$, $T_\infty = 135.35$, $T_w/T_0 = 0.24$).

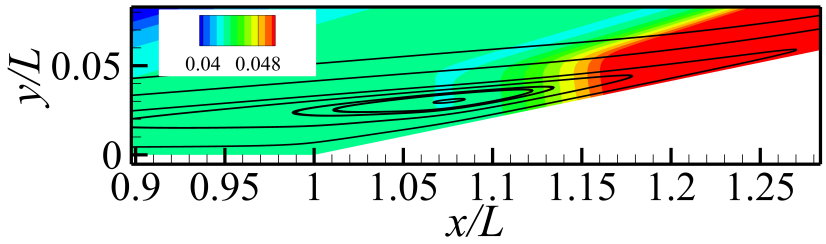

Figure 21: Non-dimensional pressure with streamlines around the compression corner ($Ma = 5.46$, $Re = 4.79\times10^6$, $\alpha = 11.7°$, $T_\infty = 123.74$, $T_w/T_0 = 0.56$).

Figure 22, it has secondary separation in the flow field. This is consistent with Hao's research [11]: as shown in Figure 10, the critical scaled ramp angle varies as a function of the wall temperature ratio, with the error bars indicating an uncertainty of 1°.

By leveraging existing physical knowledge, previous insights can be utilized to interpret the data-fused prediction outcomes.

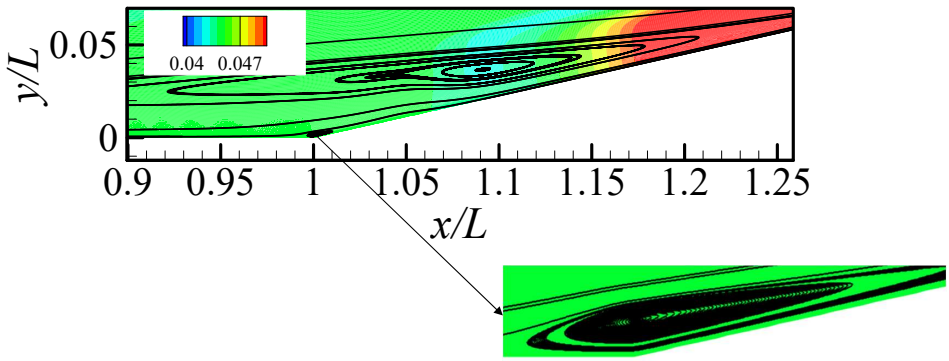

Figure 22: Non-dimensional pressure with streamlines around the compression corner with the flow conditions the same as Fig. 21 except $\alpha = 12.7°$.

5. Conclusion

This paper proposes a deep learning-based data fusion method to predict the global stability of supersonic and hypersonic compression corner flows. The model is trained on DNS data and global stability data from GSA. We show how fusing aerodynamic data from compression ramp surfaces can use small high-quality datasets to reduce data costs. We also compare different data types and train the model using only key data points selected by feature extraction. This demonstrates the importance of choosing the right data and locations for effective data fusion. The main contributions are summarized as follows:

(i) The prediction results of DA-Net trained on the small sample dataset agree well with numerical simulations across a wide range of free-stream Mach numbers, far-field flow temperatures, and ramp angles. Additionally, when this method is applied to extrapolate predictions for unseen experimental data, it still performs well.

(ii) We have observed that the data type greatly impacts the prediction results of the DA-Net method. By incorporating diverse surface coefficients (pressure or friction coefficient) as data sources for the method, we reveal a strong correlation between the data type and the underlying physical flow phenomena. Specifically, the integration of pressure coefficient has better prediction results. Therefore, we can leverage prior physical knowledge to select data for fusion effectively.

(iii) Through data feature extraction, we have discovered that by solely utilizing feature data without requiring all distribution data for the data fusion in DA-Net, we can still achieve comparable results. This also indicates that we can use prior physical knowledge to select the feature data for data fusion.

(iv) By only using the friction coefficient at the corner, reasonably accurate results can still be obtained and the model performs well for the experiments with a wide range of freestream Mach numbers, far field flow temperatures, ramp angles, Reynolds numbers and wall temperature ratios. Specifically, further analysis is conducted for cases of global instability: it is further confirmed that secondary separation occurs after global instability. Moreover, for global instability, the error in the scaled angle is within $\pm 1^{\circ}$.

Therefore, in the future, the DA-Net data fusion method will be applied to a broader range of structures, such as stability predictions for structures like the double cone. This extension aims to significantly reduce computational resources while enhancing predictive accuracy and precision.

Acknowledgements

This work is supported by Environment and Conservation Fund (ECF 29/2022), the Start-up Fund from PolyU (P0049052), the internal fund from PolyU RISport

(P0050247 and P0055369), and the Innovation and Technology Fund - Innovation and Technology Support Programme (ITF-ITSP) (ITS/062/23FP).

Conflict of Interest

The authors have no conflicts to disclose.

Data Availability Statement

The data that support the findings of this study are available from the corresponding author upon reasonable request.

Declaration of generative AI and AI-assisted technologies in the writing process

During the preparation of this work the authors used ChatGPT in order to improve language. After using this tool, the authors reviewed and edited the content as needed and take full responsibility for the content of the publication.

References

[1] D. Yibo, Y. Xiaokui, C. Guangshan, S. Jiashun, Review of control and guidance technology on hypersonic vehicle, Chinese Journal of Aeronautics 35 (7) (2022) 1–18.

[2] J. D. Schmisseur, Hypersonics into the 21st century: A perspective on afosr-sponsored research in aerothermodynamics, Progress in Aerospace Sciences 72 (2015) 3–16.

[3] P. Li, J. Ma, Z. Zheng, Robust adaptive multivariable higher-order sliding mode flight control for air-breathing hypersonic vehicle with actuator failures, International Journal of Advanced Robotic Systems 13 (5) (2016) 1729881416663376.

[4] L. Changtong, H. Zongmin, L. Yunfeng, J. Zonglin, Research progress on ground-to-flight correlation of aerodynamic force and heating data from hypersonic wind tunnels, Journal of Experiments in Fluid Mechanics 34 (3) (2020) 78–89.

[5] Z. Chen, J. Hao, C.-Y. Wen, Numerical study on the periodic control of supersonic compression corner flow using a nanosecond pulsed plasma actuator, International Journal of Heat and Mass Transfer 219 (2024) 124868.

[6] A. Roghelia, P. V. Chuvakhov, H. Olivier, I. Egorov, Experimental investigation of görtler vortices in hypersonic ramp flows behind sharp and blunt leading edges, 47th AIAA fluid dynamics conference (2017) 3463.

[7] A. Roghelia, H. Olivier, I. Egorov, P. Chuvakhov, Experimental investigation of görtler vortices in hypersonic ramp flows, Experiments in Fluids 58 (10) (2017) 139.

[8] A. J. D. Smith, The dynamic response of a wedge separated hypersonic flow and its effects on heat transfer, Ph.D. thesis, University of Southampton (1993).

[9] M. Holden, A study of flow separation in regions of shock wave-boundary layer interaction in hypersonic flow, in: 11th Fluid and PlasmaDynamics Conference, 1978, p. 1169.

[10] M. Bleilebens, H. Olivier, On the influence of elevated surface temperatures on hypersonic shock wave/boundary layer interaction at a heated ramp model, Shock Waves 15 (5) (2006) 301–312.

[11] J. Hao, S. Cao, C.-Y. Wen, H. Olivier, Occurrence of global instability in hypersonic compression corner flow, Journal of Fluid Mechanics 919 (2021) A4.

[12] S. Cao, J. Hao, I. Klioutchnikov, H. Olivier, C.-Y. Wen, Unsteady effects in a hypersonic compression ramp flow with laminar separation, Journal of Fluid Mechanics 912 (2021) A3.

[13] J. Fan, J. Hao, C.-Y. Wen, Role of very large-scale motions in shock wave/turbulent boundary layer interactions, Physics of Fluids 36 (8) (2024).

[14] G. S. Settles, I. E. Vas, S. M. Bogdonoff, Details of a shock-separated turbulent boundary layer at a compression corner, AIAA journal 14 (12) (1976) 1709–1715.

[15] J. Poggie, Effect of forcing on a supersonic compression ramp flow, AIAA Journal 57 (9) (2019) 3765–3772.

[16] J. Tao, G. Sun, Application of deep learning based multi-fidelity surrogate model to robust aerodynamic design optimization, Aerospace Science and Technology 92 (2019) 722–737.

[17] Y. Mack, T. Goel, W. Shyy, R. Haftka, Surrogate model-based optimization framework: a case study in aerospace design, Evolutionary computation in dynamic and uncertain environments (2007) 323–342.

[18] V. Hassija, V. Chamola, A. Mahapatra, A. Singal, D. Goel, K. Huang, S. Scardapane, I. Spinelli, M. Mahmud, A. Hussain, Interpreting black-box models: a review on explainable artificial intelligence, Cognitive Computation 16 (1) (2024) 45–74.

[19] Y. Dong, J. Tao, Y. Zhang, W. Lin, J. Ai, Deep learning in aircraft design, dynamics, and control: Review and prospects, IEEE Transactions on Aerospace and Electronic Systems 57 (4) (2021) 2346–2368.

[20] K. Poulinakis, D. Drikakis, I. W. Kokkinakis, S. M. Spottswood, Deep learning reconstruction of pressure fluctuations in supersonic shock–boundary layer interaction, Physics of Fluids 35 (7) (2023).

[21] Y. Guo, S. Mahadevan, S. Matsumoto, S. Taba, D. Watanabe, Investigation of surrogate modeling options with high-dimensional input and output, AIAA Journal 61 (3) (2023) 1334–1348.

[22] S. K. Ravi, A. Bhaduri, A. Amer, S. Ghosh, L. Wang, A. Hoffman, R. Umretiya, I. Roy, R. Rebak, V. S. Dheeradhada, et al., On uncertainty quantification in materials modeling and discovery: Applications of ge's bhm and idace, in: AIAA SCITECH 2023 Forum, 2023.

[23] L. Nugroho, R. Akmeliawati, Comparison of black-grey-white box approach in system identification of a flight vehicle, in: Journal of Physics: Conference Series, Vol. 1130, IOP Publishing, 2018, p. 012024.

[24] Y. Zhu, N. Zabaras, P.-S. Koutsourelakis, P. Perdikaris, Physics-constrained deep learning for high-dimensional surrogate modeling and uncertainty

quantification without labeled data, Journal of Computational Physics 394 (2019) 56–81.

[25] G. E. Karniadakis, I. G. Kevrekidis, L. Lu, P. Perdikaris, S. Wang, L. Yang, Physics-informed machine learning, Nature Reviews Physics 3 (6) (2021) 422–440.

[26] C. Zhang, C.-Y. Wen, Y. Jia, Y.-H. Juan, Y.-T. Lee, Z. Chen, A.-S. Yang, Z. Li, Enhancing the accuracy of physics-informed neural networks for indoor airflow simulation with experimental data and reynolds-averaged navier–stokes turbulence model, Physics of Fluids 36 (6) (2024).

[27] J. Kou, C. Ning, W. Zhang, Transfer learning for flow reconstruction based on multifidelity data, AIAA Journal 60 (10) (2022) 5821–5842.

[28] C. Lu, S. Wang, X. Wang, A multi-source information fusion fault diagnosis for aviation hydraulic pump based on the new evidence similarity distance, Aerospace Science and Technology 71 (2017) 392–401.

[29] B. Yang, B. Chen, Y. Liu, J. Chen, Gaussian process fusion method for multi-fidelity data with heterogeneity distribution in aerospace vehicle flight dynamics, Engineering Applications of Artificial Intelligence 138 (2024) 109228.

[30] T. Zhigong, Y. Xianxu, Q. Weiqi, X. Hanshan, B. Lin, W. Wenzheng, Research progress on the fusion of data obtained by high-speed wind tunnels, cfd and model flight, Acta Aerodynamica Sinica 41 (8) (2023) 44–58.

[31] L. He, W. Qian, T. Zhao, Q. Wang, Multi-fidelity aerodynamic data fusion with a deep neural network modeling method, Entropy 22 (9) (2020) 1022.

[32] K. Li, J. Kou, W. Zhang, Deep learning for multifidelity aerodynamic distribution modeling from experimental and simulation data, AIAA Journal 60 (7) (2022) 4413–4427.

[33] C. Ning, W. Zhang, Mha-net: Multi-source heterogeneous aerodynamic data fusion neural network embedding reduced-dimension features, Aerospace Science and Technology 145 (2024) 108908.

[34] J. Hao, J. Wang, C. Lee, Numerical study of hypersonic flows over reentry configurations with different chemical nonequilibrium models, Acta Astronautica 126 (2016) 1–10.

[35] J. Hao, C.-Y. Wen, Hypersonic flow over spherically blunted double cones, Journal of Fluid Mechanics 896 (2020) A26.

[36] J. Hao, S. Cao, P. Guo, C.-Y. Wen, Response of hypersonic compression corner flow to upstream disturbances, Journal of Fluid Mechanics 964 (2023) A25.

[37] V. Theofilis, S. Hein, U. Dallmann, On the origins of unsteadiness and three-dimensionality in a laminar separation bubble, Philosophical Transactions of the Royal Society of London. Series A: Mathematical, Physical and Engineering Sciences 358 (1777) (2000) 3229–3246.

[38] J.-C. Robinet, Bifurcations in shock-wave/laminar-boundary-layer interaction: global instability approach, Journal of Fluid Mechanics 579 (2007) 85–112.

[39] V. Theofilis, Global linear instability, Annual Review of Fluid Mechanics 43 (1) (2011) 319–352.

[40] N. Hildebrand, A. Dwivedi, J. W. Nichols, M. R. Jovanović, G. V. Candler, Simulation and stability analysis of oblique shock-wave/boundary-layer interactions at mach 5.92, Physical Review Fluids 3 (1) (2018) 013906.

[41] M. D. Shields, J. Zhang, The generalization of latin hypercube sampling, Reliability Engineering & System Safety 148 (2016) 96–108.

[42] D. P. Kingma, Adam: A method for stochastic optimization, arXiv preprint arXiv:1412.6980 (2014).

[43] K. Stewartson, P. Williams, Self-induced separation, Proceedings of the Royal Society of London. A. Mathematical and Physical Sciences 312 (1509) (1969) 181–206.

[44] V. Y. Neiland, Theory of laminar boundary layer separation in supersonic flow, Fluid Dynamics 4 (4) (1969) 33–35.

[45] S. Gs, A. Dwivedi, G. V. Candler, J. W. Nichols, Onset of three-dimensionality in supersonic flow over a slender double wedge, Physical Review Fluids 3 (9) (2018) 093901.

[46] I. Egorov, V. Neiland, V. Shredchenko, Three-dimensional flow structures at supersonic flow over the compression ramp, in: 49th AIAA Aerospace Sciences Meeting including the New Horizons Forum and Aerospace Exposition, 2011, p. 730.

[47] S. Cao, I. Klioutchnikov, H. Olivier, Görtler vortices in hypersonic flow on compression ramps, AIAA Journal 57 (9) (2019) 3874–3884.

673 [48] A. Durna, B. Celik, Effects of double-wedge aft angle on hypersonic laminar
674 flows, AIAA Journal 58 (4) (2020) 1689–1703.

675 [49] L. Antwarg, R. M. Miller, B. Shapira, L. Rokach, Explaining anomalies de-
676 tected by autoencoders using shapley additive explanations, Expert systems
677 with applications 186 (2021) 115736.